

Uncertainty characterization of particle depth measurement using digital in-line holography and the hybrid method

Jian Gao,¹ Daniel R. Guildenbecher,² Phillip L. Reu,² and Jun Chen^{1,*}

¹School of Mechanical Engineering, Purdue University, West Lafayette, IN 47907, USA

²Sandia National Laboratories, Albuquerque, NM 87185, USA

junchen@purdue.edu

Abstract: In the detection of particles using digital in-line holography, measurement accuracy is substantially influenced by the hologram processing method. In particular, a number of methods have been proposed to determine the out-of-plane particle depth (z location). However, due to the lack of consistent uncertainty characterization, it has been unclear which method is best suited to a given measurement problem. In this work, depth determination accuracies of seven particle detection methods, including a recently proposed hybrid method, are systematically investigated in terms of relative depth measurement errors and uncertainties. Both synthetic and experimental holograms of particle fields are considered at conditions relevant to particle sizing and tracking. While all methods display a range of particle conditions where they are most accurate, in general the hybrid method is shown to be the most robust with depth uncertainty less than twice the particle diameter over a wide range of particle field conditions.

© 2013 Optical Society of America

OCIS codes: (090.1995) Digital holography; (120.0120) Instrumentation, measurement, and metrology; (100.6890) Three-dimensional image processing; (350.4990) Particles.

References and links

1. H. Meng, G. Pan, Y. Pu, and S. H. Woodward, "Holographic particle image velocimetry: from film to digital recording," *Meas. Sci. Technol.* **15**, 673 (2004).
2. J. Sheng, E. Malkiel, and J. Katz, "Using digital holographic microscopy for simultaneous measurements of 3D near wall velocity and wall shear stress in a turbulent boundary layer," *Exp. Fluids* **45**, 1023–1035 (2008).
3. D. Chareyron, J. L. Marié, C. Fournier, J. Gire, N. Grosjean, L. Denis, M. Lance, and L. Méès, "Testing an in-line digital holography inverse method for the Lagrangian tracking of evaporating droplets in homogeneous nearly isotropic turbulence," *New J. Phys.* **14**, 043039 (2012).
4. N. A. Buchmann, C. Atkinson, and J. Soria, "Ultra-high-speed tomographic digital holographic velocimetry in supersonic particle-laden jet flows," *Meas. Sci. Technol.* **24**, 024005 (2013).
5. J. Lee, K. A. Sallam, K. C. Lin, and C. D. Carter, "Spray structure in near-injector region of aerated jet in subsonic crossflow," *J. Propul. Power* **25**, 258–266 (2009).
6. Q. Lü, Y. Chen, R. Yuan, B. Ge, Y. Gao, and Y. Zhang, "Trajectory and velocity measurement of a particle in spray by digital holography," *Appl. Opt.* **48**, 7000–7007 (2009).
7. Y. Yang and B. seon Kang, "Digital particle holographic system for measurements of spray field characteristics," *Opt. Laser Eng.* **49**, 1254–1263 (2011).
8. J. Gao, D. R. Guildenbecher, P. L. Reu, V. Kulkarni, P. E. Sojka, and J. Chen, "Quantitative, three-dimensional diagnostics of multiphase drop fragmentation via digital in-line holography," *Opt. Lett.* **38**, 1893–1895 (2013).
9. J. Sheng, E. Malkiel, J. Katz, J. Adolf, R. Belas, and A. R. Place, "Digital holographic microscopy reveals prey-induced changes in swimming behavior of predatory dinoflagellates," *Proc. Nat. Acad. Sci. USA* **104**, 17512–17517 (2007).

10. S. J. Lee, K. W. Seo, Y. S. Choi, and M. H. Sohn, "Three-dimensional motion measurements of free-swimming microorganisms using digital holographic microscopy," *Meas. Sci. Technol.* **22**, 064004 (2011).
11. L. Tian, N. Loomis, J. A. Domínguez-Caballero, and G. Barbastathis, "Quantitative measurement of size and three-dimensional position of fast-moving bubbles in air-water mixture flows using digital holography," *Appl. Opt.* **49**, 1549–1554 (2010).
12. D. Lebrun, D. Allano, L. Méès, F. Walle, F. Corbin, R. Boucheron, and D. Fréchou, "Size measurement of bubbles in a cavitation tunnel by digital in-line holography," *Appl. Opt.* **50**, H1–H9 (2011).
13. J. P. Fugal, R. A. Shaw, E. W. Saw, and A. V. Sergeyev, "Airborne digital holographic system for cloud particle measurements," *Appl. Opt.* **43**, 5987–5995 (2004).
14. Y.-S. Choi and S.-J. Lee, "Three-dimensional volumetric measurement of red blood cell motion using digital holographic microscopy," *Appl. Opt.* **48**, 2983–2990 (2009).
15. T. Khanam, M. N. Rahman, A. Rajendran, V. Kariwala, and A. K. Asundi, "Accurate size measurement of needle-shaped particles using digital holography," *Chem. Eng. Sci.* **66**, 2699–2706 (2011).
16. S. Murata and N. Yasuda, "Potential of digital holography in particle measurement," *Opt. Laser Technol.* **32**, 567–574 (2000).
17. J. Sheng, E. Malkiel, and J. Katz, "Digital holographic microscope for measuring three-dimensional particle distributions and motions," *Appl. Opt.* **45**, 3893–3901 (2006).
18. V. Ilchenko, T. Lex, and T. Sattelmayer, "Depth position detection of the particles in digital holographic particle image velocimetry (DHPIV)," *Proc. SPIE* **5851**, 123–128 (2005).
19. J. P. Fugal, T. J. Schulz, and R. A. Shaw, "Practical methods for automated reconstruction and characterization of particles in digital in-line holograms," *Meas. Sci. Technol.* **20**, 075501 (2009).
20. Y. Yang, G. Li, L. Tang, and L. Huang, "Integrated gray-level gradient method applied for the extraction of three-dimensional velocity fields of sprays in in-line digital holography," *Appl. Opt.* **51**, 255–267 (2012).
21. Y. Wu, X. Wu, Z. Wang, L. Chen, and K. Cen, "Coal powder measurement by digital holography with expanded measurement area," *Appl. Opt.* **50**, H22–H29 (2011).
22. D. R. Guildenbecher, J. Gao, P. L. Reu, and J. Chen, "Digital holography simulations and experiments to quantify the accuracy of 3D particle location and 2D sizing using a proposed hybrid method," *Appl. Opt.* **52**, 3790–3801 (2013).
23. V. Palero, M. Arroyo, and J. Soria, "Digital holography for micro-droplet diagnostics," *Exp. Fluids* **43**, 185–195 (2007).
24. E. Darakis, T. Khanam, A. Rajendran, V. Kariwala, T. J. Naughton, and A. K. Asundi, "Microparticle characterization using digital holography," *Chem. Eng. Sci.* **65**, 1037–1044 (2010).
25. Y. Yang, B. seon Kang, and Y. jun Choo, "Application of the correlation coefficient method for determination of the focal plane to digital particle holography," *Appl. Opt.* **47**, 817–824 (2008).
26. G. Pan and H. Meng, "Digital holography of particle fields: Reconstruction by use of complex amplitude," *Appl. Opt.* **42**, 827–833 (2003).
27. W. Yang, A. B. Kostinski, and R. A. Shaw, "Phase signature for particle detection with digital in-line holography," *Opt. Lett.* **31**, 1399–1401 (2006).
28. F. Dubois, C. Schockaert, N. Callens, and C. Yourassowsky, "Focus plane detection criteria in digital holography microscopy by amplitude analysis," *Opt. Express* **14**, 5895–5908 (2006).
29. C. Buraga-Lefebvre, S. Coëtmellec, D. Lebrun, and C. Özkul, "Application of wavelet transform to hologram analysis: three-dimensional location of particles," *Opt. Laser Eng.* **33**, 409–421 (2000).
30. S. Soontaranon, J. Widjaja, and T. Asakura, "Extraction of object position from in-line holograms by using single wavelet coefficient," *Opt. Commun.* **281**, 1461–1467 (2008).
31. F. Soulez, L. Denis, C. Fournier, Éric Thiébaut, and C. Goepfert, "Inverse-problem approach for particle digital holography: accurate location based on local optimization," *J. Opt. Soc. Am. A* **24**, 1164–1171 (2007).
32. J. W. Goodman, *Introduction to Fourier Optics* (McGraw-Hill, 1996).
33. F. Slimani, G. Grehan, G. Gouesbet, and D. Allano, "Near-field Lorenz-Mie theory and its application to micro-holography," *Appl. Opt.* **23**, 4140–4148 (1984).
34. D. K. Singh and P. K. Panigrahi, "Improved digital holographic reconstruction algorithm for depth error reduction and elimination of out-of-focus particles," *Opt. Express* **18**, 2426–2448 (2010).

Nomenclature

A_r	reconstructed amplitude
D_0	actual particle diameter
D_d	measured particle diameter
D_I	depth map of I_{min}
D_T	depth map of T_{max}

E_r	reconstructed complex amplitude
EE	set of exterior-edge pixels
F	Fresnel number
$h(m, n)$	intensity distribution of a digital hologram
I_{min}	minimum intensity map
I_r	reconstructed intensity
IE	set of interior-edge pixels
k, l	discrete coordinates in the image plane
lap	Laplacian kernel
L	distance between the hologram plane and the nearest surface of a particle field
m, n	discrete coordinates in the hologram plane
m', n'	discrete coordinates in the spatial frequency domain
M, N	number of pixels in the x and y directions
P	set of pixels that belong to a particle
S	quantified sharpness
S_x, S_y	horizontal and vertical Sobel kernels
t	threshold
T	Tenengrad map
T_{max}	maximum Tenengrad map
W	set of pixels that belong to a local window
z_0	actual particle distance
z_d	measured particle distance
z_r	reconstruction distance
δ_z	depth uncertainty
ΔC_z	correlation interval
Δz_0	actual displacement
Δz_d	measured displacement
$\Delta\xi, \Delta\eta$	dimension of an individual pixel in the x and y directions
λ	wavelength
ρ_n	particle number density
\mathcal{E}	edge finding operation
\mathcal{F}	fast Fourier transform
\mathcal{F}^{-1}	inverse fast Fourier transform
\mathcal{T}	thresholding operation

1. Introduction

Digital in-line holography (DIH) has been extensively applied to the detection and characterization of particle fields, where the particles can be tracer particles in flow measurements [1–4], droplets in spray diagnostics [5–8], micro-organisms in biological mobility studies [9, 10], bubbles in multiphase flows [11, 12] and other particles of interest [13–15]. Besides the simplicity of the in-line setup, the accessibility to three-dimensional (3D) information has promoted the application of DIH, in which the particle size, shape and 3D location can be measured. Furthermore, 3D, three-component velocities can be determined by pairing particles detected in sequential holograms.

The performance of DIH relies heavily on the accuracy of the measured particle depth (z location). Reconstruction at an accurate depth gives a well-focused particle image and ensures precise extraction of the particle's size, shape and transverse location (x - y location). In addition to hardware issues (e.g., low pixel resolution of digital cameras) that affect the accuracy of particle detection, the methods (algorithms) to extract the depth also have a remarkable influence

on the measurement accuracy.

Various methods have been developed to process in-line holograms, and methods to determine particle depth can be broadly grouped into three categories. The first category includes methods that utilize the reconstructed intensity (amplitude) image of the particle. The presumption is that when the hologram of a particle is reconstructed at the particle's true depth, i.e., focal plane of the particle, the focus criterion reaches its extremum. In the reconstruction of particle holograms without filtering of the DC term, the focused image of a particle appears as a dark region with sharp edges in contrast to the bright background. For this reason, the minimum intensity of a reconstructed particle image is commonly used as a focus criterion [15–17]. Specifically, the particle depth is determined by locating the z -position where the particle image intensity reaches a minimum. Similarly, the depth may also be found by maximizing a sharpness index applied to the reconstructed particle image [14, 18–22]. Furthermore, assuming the focused particle image has an even intensity distribution, the minimum variance may also be used as a focus indicator [23, 24]. Additionally, symmetry of the out of focus images about the in-focus z position has been utilized by Yang et al. [25] to find the depth by maximizing a correlation coefficient (CC) of the particle images reconstructed before and after the focus position. Finally, the HYBRID method [22] is a new method which has recently been proposed by the authors. In-focus particles are found by searching for regions with a minimum intensity and maximum edge sharpness. Particular advantages of the HYBRID method include automatic selection of thresholds for image segmentation, precise determination of the in-plane (x - y plane) shape, and suitability to particles of arbitrary shapes.

The second category includes approaches that use the complex amplitude information of the reconstructed light field. For example, Pan and Meng [26] use the dip position in the root mean square (RMS) value of the imaginary part of the reconstructed complex amplitude as the focus position. Yang et al. [27] discover a phase signature near the particle focus depth and locate a particle by searching for this phase signature in the depth direction. Dubois et al. [28] determine that the integrated amplitude of the reconstructed wave reaches a minimum for pure amplitude objects and achieves a maximum for pure phase objects at the focal plane of the object.

Finally, the third category includes methods that determine the depth by analyzing the interference pattern without reconstruction of the holograms. The wavelet analysis has been applied to the detection of particle size and location [29, 30]. Also, Soulez et al. [31] propose a depth refinement method by looking for the set of particle parameters at which the discrepancies between the model and the experimental data are minimized statistically.

Among the aforementioned works, methods used to determine measurement accuracy are inconsistent. Consequently, a systematic comparison of method accuracy is difficult, and it remains unclear which method is best suited to a given measurement problem. To conduct a systematic characterization of measurement accuracy, both synthetic and experimental holograms of particles are needed. Results obtained from synthetic holograms, which do not include all experimental noise sources, can be considered to give an estimation of the optimal performance of a method. On the other hand, results obtained from experimental holograms are necessary to investigate the influence of realistic noise sources on detection accuracy.

This work focuses on applications of DIH for simultaneous measurement of particle position and size. The range of conditions investigated is selected based on recent applications [7, 8, 11, 23] and current sensor technology. In general particle sizes are significantly larger than the pixel size, which allows for extraction of particle morphology from in-focus images. Note, for applications where tracer particles are utilized in flow measurements (e.g., holographic particle image velocimetry, HPIV), particle sizes are often on the order of pixel sizes. In that case, accurate particle sizing is typically not of interest and alternative depth retrieval method are often utilized [17, 26, 34]. This work is not intended to address such ap-

plications. Further note, as is often the case in the literature for applications of DIH to particle sizing and tracking [11, 20], some of the conditions explored here violate the critical recording distance, defined in [34]. Consequently fringes near the hologram borders are not fully resolved. More work is needed to determine if the critical recording distance, which was originally developed for HPIV applications, can or should be applied for situations where the particle size is much greater than the pixel size.

In the present study, the measurement accuracy of the HYBRID method is quantified in terms of relative depth error and depth uncertainty using both synthetic and experimental holograms. Considering comparability and the amount of coding needed, we also quantify the accuracies of six alternative methods, which belong to the first category of particle detection methods. The HYBRID method and the alternative methods are described after a brief introduction to the technique of DIH. This is followed by the numerical and experimental quantification of measurement accuracy and the conclusions.

2. Introduction to DIH

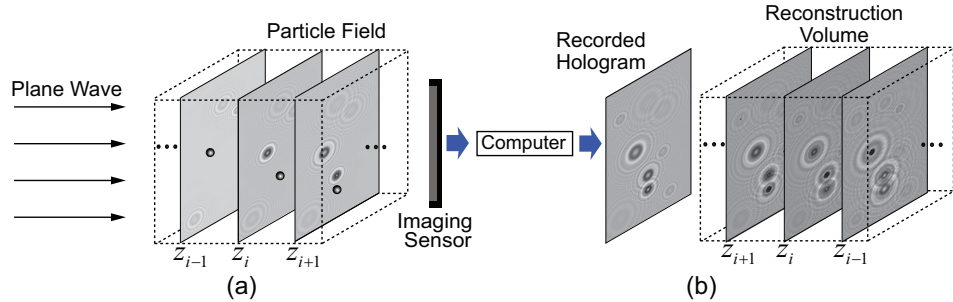


Fig. 1. DIH for particle field detection: (a) recording and (b) reconstruction.

The schematic of DIH for particle detection is shown in Fig. 1. In the recording step, a plane wave illuminates the particles, and the hologram is formed by the interference between the light scattered off the particles (object wave) and the undisturbed part of the illuminating light (reference wave). The hologram is recorded as a digital grayscale image $h(m, n)$ by an imaging sensor (CCD or CMOS) and stored in a computer. In the reconstruction step, the Rayleigh-Sommerfeld diffraction equation is evaluated numerically to simulate the analog reconstruction process in which the reference wave illuminates the hologram and further propagates to a reconstruction plane forming the reconstructed image. The numerically reconstructed complex amplitude E_r can be expressed as

$$E_r(k, l, z_r) = \mathcal{F}^{-1} \{ \mathcal{F} \{ h(m, n) \} G(m', n', z_r) \}. \quad (1)$$

$$G(m', n', z_r) = \exp \left(j \frac{2\pi}{\lambda} z_r \sqrt{1 - \left(\frac{\lambda m'}{M \Delta \xi} \right)^2 - \left(\frac{\lambda n'}{N \Delta \eta} \right)^2} \right) \text{circ} \left(\sqrt{\left(\frac{\lambda m'}{M \Delta \xi} \right)^2 + \left(\frac{\lambda n'}{N \Delta \eta} \right)^2} \right) \quad (2)$$

is the discrete analytical expression for the Fourier transform of the Rayleigh-Sommerfeld diffraction kernel [32]. The reconstructed amplitude is $A_r = |E_r|$, and the reconstructed intensity is $I_r = |E_r|^2$. One advantage of numerical reconstruction is digital focusing, in which particles at different depths can be brought into focus by altering the value of z_r during reconstruction using Eq. (1), as shown in Fig. 1(b). Accordingly, the depth at which a particle is in focus is determined as the z coordinate of the particle. Further, the transverse (x and y) coordinates and in-plane size and shape of the particle can be evaluated from the focused image of the particle.

3. Hybrid method for particle field detection

The HYBRID method was recently proposed in [22]. Here, further details of the method implementation are given. This method uses the edge sharpness in conjunction with the image intensity to realize automatic selection of segmentation thresholds and optimized detection of particle binary images. Depth is determined by maximizing the edge sharpness. Four steps are involved in the implementation of the method.

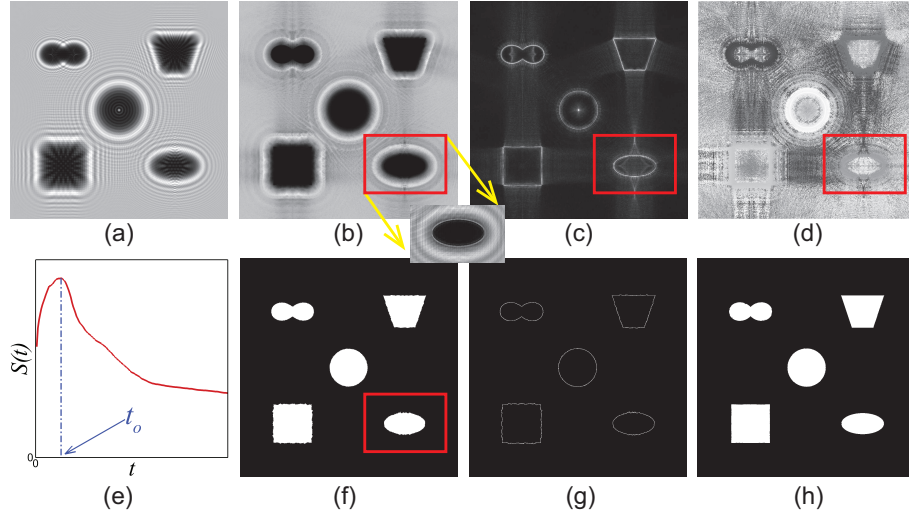


Fig. 2. Illustration of the HYBRID method. (a) synthetic in-line hologram. (b) $I_{min}(k,l)$. (c) $T_{max}(k,l)$. (d) $D_T(k,l)$. (e) global sharpness profile. (f) $\mathcal{T}_{t_o}\{I_{min}\}$. (g) $\mathcal{E}\{\mathcal{T}_{t_o}\{I_{min}\}\}$. (h) refined particle binary images. Inset: Local intensity $I_r(k,l,z'_d)$

The first step is volume reconstruction of the hologram to obtain the minimum intensity map, I_{min} , maximum Tenengrad map, T_{max} and its depth map, D_T , as shown in Figs. 2(a)-2(d). These are expressed mathematically as

$$I_{min}(k,l) = \min_{z_r} I_r(k,l,z_r) \quad (3)$$

$$T_{max}(k,l) = \max_{z_r} T(k,l,z_r) \quad (4)$$

$$D_T(k,l) = \arg \max_{z_r} T(k,l,z_r). \quad (5)$$

$T(k,l,z_r)$ is the sharpness of the reconstructed image, quantified by the Tenengrad operator, which can be expressed as

$$T(k,l,z_r) = [A_r(k,l,z_r) \otimes S_x]^2 + [A_r(k,l,z_r) \otimes S_y]^2, \quad (6)$$

where S_x and S_y are the horizontal and vertical Sobel kernels, respectively. The depth range ($z_{min} \leq z_r \leq z_{max}$) for the volume reconstruction is established such that the particles of interest are enclosed. It is assumed that the interval between consecutive depths is small enough to neglect its influence on the measurement accuracy.

The second step is segmentation of the particle field by thresholding I_{min} using an automatically selected threshold. Symbol $\mathcal{T}_t\{\cdot\}$ denotes the thresholding operation using a threshold t , which results in a binary image, as illustrated in Fig. 2(f). Symbol $\mathcal{E}\{\cdot\}$ denotes an operation that finds the exterior edge pixels (exterior contours) of binary segments, which can be realized

by subtracting the original binary image from the morphologically dilated binary image. Figure 2(g) shows the $\mathcal{E}\{\cdot\}$ operation applied to the binary image in Fig. 2(f). An optimal threshold is selected from a sequence of tentative thresholds bounded by the minimum and maximum values in I_{min} . The selection process is automated using the global sharpness $S(t)$ at each tentative threshold t , which is defined as

$$S(t) = \frac{\sum_{k,l} (\mathcal{E}\{\mathcal{T}_t\{I_{min}\}\} \cdot T_{max})}{\sum_{k,l} \mathcal{E}\{\mathcal{T}_t\{I_{min}\}\}}, \quad (7)$$

where \cdot denotes pointwise multiplication. The profile of $S(t)$ achieved from Figs. 2(b) and 2(c) is shown in Fig. 2(e). t_o is selected from the maximum value of $S(t)$ and defines the optimal threshold, at which the particle segments (Fig. 2(f)) are separated from each other and easily identified.

The third step refines the detection of each particle. According to the size and in-plane (x - y) location information of the segments obtained in the second step, rectangular local windows are defined to enclose individual particles, as indicated by the red rectangles in Fig. 2. The typical size of a local window is twice that of the segment enclosed. Next, the procedures in the second step are applied locally in each window to find the optimal threshold for each particle. Specifically, the optimal threshold for a particle, t'_o , is obtained by maximizing the local sharpness, $S_W(t)$, expressed as

$$S_W(t) = \frac{\sum_{k,l \in W} (\mathcal{E}\{\mathcal{T}_t\{I_{min}\}\} \cdot T_{max})}{\sum_{k,l \in W} \mathcal{E}\{\mathcal{T}_t\{I_{min}\}\}}, \quad (8)$$

where W is the set of pixels that belong to the window. The edge pixels are identified by $\mathcal{E}\{\mathcal{T}_{t'_o}\{I_{min}\}\}$. Assuming that the edge sharpness is maximized when the particle is in focus, the z location is estimated by conditionally averaging the depths of the edge pixels (according to D_T). To exclude potential outliers during the averaging, the edge pixels, whose sharpness values are less than half of the maximum sharpness value in the window (according to T_{max}), are eliminated. An initial depth z'_d is then determined by taking the mean of the depths of the rest of edge pixels.

The fourth step is further refinement of the measurement using the local intensity. After the hologram is reconstructed at z'_d , a new optimal threshold, t''_o , is decided by replacing I_{min} in Eq. (8) with the local intensity, $I_r(k,l,z'_d)$. The final depth, z_d , is determined for the particle, following the procedure in the third step. Since the local intensity, shown in the inset in Fig. 2, describes the particle better than I_{min} , the refined particle binary image with smooth contours is obtained by thresholding the local intensity with t''_o , as shown in Fig. 2(h). Further, the transverse location, in-plane size and shape of the particle can be measured from the refined binary image.

4. Alternative particle detection methods

In addition to the HYBRID method, six other particle detection methods are tested in order to evaluate the accuracy of each method and determine the measurement problems to which they are best suited. Below is a brief introduction to these methods.

Laplacian (LAP) method

The LAP method [14] locates a particle in the z direction by maximizing the sum of squared Laplacian values in an investigation window enclosing the particle. The LAP value can be

expressed as

$$LAP(z_r) = \sum_{k,l \in W} [I_r(k,l,z_r) \otimes lap]^2, \quad (9)$$

where

$$lap = \begin{pmatrix} 0 & 1 & 0 \\ 1 & -4 & 1 \\ 0 & 1 & 0 \end{pmatrix} \quad (10)$$

is the Laplacian kernel. Then, the particle depth z_d is determined by maximizing $LAP(z_r)$. In the present study, the size of the window is twice that of the particle enclosed.

Correlation coefficient (CC) method

The CC method [25] finds the particle depth by maximizing the CC value along the z direction, which can be written as

$$CC(z_r) = \frac{\sum_{k,l \in W} [C(k,l,z_r - \Delta C_z/2)C(k,l,z_r + \Delta C_z/2)]}{\sqrt{\sum_{k,l \in W} [C(k,l,z_r - \Delta C_z/2)]^2 \sum_{k,l \in W} [C(k,l,z_r + \Delta C_z/2)]^2}}, \quad (11)$$

where $C(k,l,z_r) = I_r(k,l,z_r) - \bar{I}_W(z_r)$, and $\bar{I}_W(z_r)$ is the mean intensity in the window. ΔC_z is the correlation interval, which is set to 1 cm [25]. For the CC method, the size of the window is 3 times that of the particle enclosed.

Variance (VAR) method

A focused particle image tends to have a uniform intensity distribution, based on which the z location can be determined by minimizing the variance of the intensity of the particle [23, 24]. This can be calculated by

$$VAR(z_r) = \frac{1}{N_P} \sum_{k,l \in P} [I_r(k,l,z_r) - \bar{I}_P(z_r)]^2, \quad (12)$$

where P is the set of pixels that belong to the particle, N_P is the number of the particle pixels, and $\bar{I}_P(z_r)$ is mean intensity of the particle.

Minimum intensity (MINI) method

By minimizing the mean intensity of the particle, the depth of a particle can be determined as [15]

$$z_d = \arg \min_{z_r} \left[\frac{1}{N_P} \sum_{k,l \in P} I_r(k,l,z_r) \right]. \quad (13)$$

Minimum edge intensity (MINEI) method

Similar to the MINI method, the average depth of the edge pixels has been used to estimate the particle depth [11], which can be obtained by

$$z_d = \frac{1}{N_{IE}} \sum_{k,l \in IE} D_I(k,l), \quad (14)$$

where

$$D_I(k,l) = \arg \min_{z_r} I_r(k,l,z_r) \quad (15)$$

is the depth map for $I_{min}(k,l)$. IE is the set of interior-edge pixels, which is a subset of P . N_{IE} is the number of interior-edge pixels.

Integrated gradient (IG) method

In the IG method, there are two focus criteria [20], which are both based on the difference between the average intensity of the particle image and that of the background. According to the particle diameter and distance, one of the criteria is selected and maximized to locate the particle in the z direction. The first criterion $IG_1(z_r)$ is defined as

$$IG_1(z_r) = \frac{1}{N_{EE}} \sum_{k,l \in EE} I_r(k,l,z_r) - \frac{1}{N_E} \sum_{k,l \in IE} I_r(k,l,z_r), \quad (16)$$

where EE is the set of exterior-edge pixels, which are the background pixels that just encompasses the particle. N_{EE} is the number of exterior-edge pixels. The second criterion $IG_2(z_r)$ is defined as

$$IG_2(z_r) = \frac{1}{N_{EE}} \sum_{k,l \in EE} I_r(k,l,z_r) - \frac{1}{N_P} \sum_{k,l \in P} I_r(k,l,z_r). \quad (17)$$

To implement the alternative methods, knowledge of the pixels that belong to the particle (or the particle binary image) is required. Therefore, in the processing of synthetic holograms, the alternative methods work on the exact particle pixels. This eliminates the effects of inaccurate particle binary images, such that the synthetic results give the optimum performance of the methods. In contrast, in the processing of experimental holograms, the exact particle information is not available. Since the HYBRID method is able to determine the particle binary image with a good degree of accuracy (Fig. 2), the alternative methods are implemented according to the particle pixels detected by the HYBRID method. Note, no pre-processing of the hologram, such as DC filtering and noise reduction, is conducted for both synthetic and experimental holograms, before implementing the particle detection methods.

5. Quantification of measurement accuracy by synthetic holograms

In this section, particle detection methods are applied to synthetic holograms, and results are compared with the particle parameters used for hologram simulation.

5.1. Accuracy in detecting a single particle

The results obtained from detection of a single particle represent the ideal performance of a particle detection method, because the hologram is free of experimental noises, e.g., diffraction patterns due to dusts on optics, aberrations in the planar wavefront, interference between light scattered by different particles, etc.

Holograms of particles with circular and square cross-sections are simulated at different particle sizes and distances. The particles are of diameter $D_0 = 40, 70, 100, 130, 160, 200, 230$ and $270 \mu\text{m}$. Each of them is located at $z_0 = 0.05, 0.10, 0.15, 0.20, 0.25$ and 0.30 m from the hologram plane. The diameter of a square is that of a circle with an equivalent area. Here, the approach used in [22], which is based on Fresnel diffraction theory, is adopted to simulate holograms of single opaque particles. Note, when Fresnel number $F = D_0^2/4\lambda z_0$ is less than 0.16, the results are also applicable to transparent particles [33] due to the fact that internal reflections and refractions have little effect on the hologram at large distances. The wavelength is 532 nm . The size of the hologram is 1024×1024 with $7.4 \times 7.4 \mu\text{m}^2$ pixels. A single particle is centered in the hologram. Some of the effects introduced by digital recording, such as digitization and readout noise, are also incorporated in the simulation. The intensity of each pixel obtained from the analytical expression is scaled linearly to the range $[0, 9830]$ and then digitized by rounding to the nearest integer. Normally distributed random noise with a standard deviation of 164 is added to each pixel. This procedure is analogous to an experimental hologram recorded by a 14-bit digital camera with the brightest pixel having a grayscale value

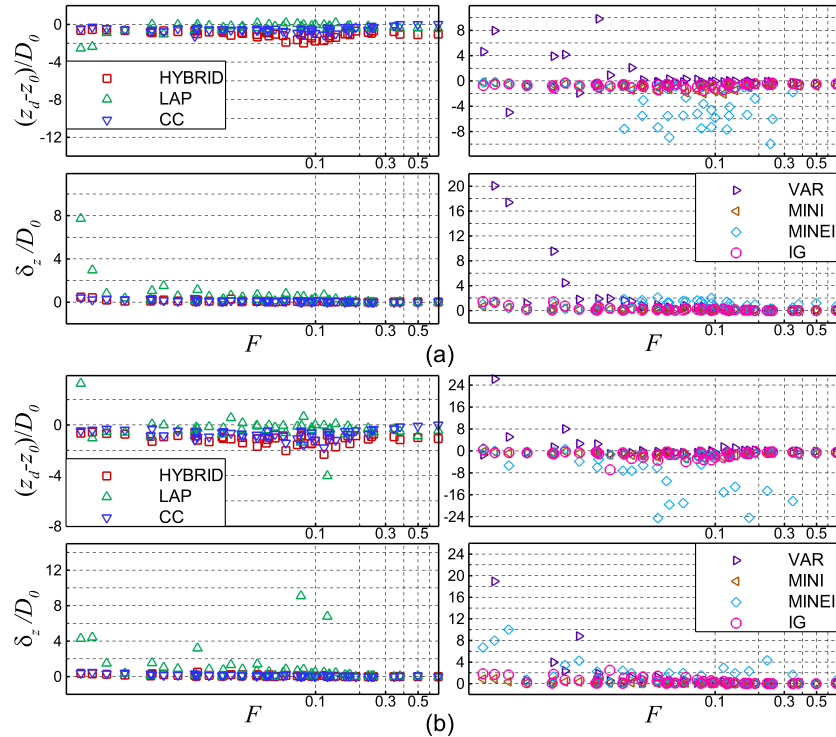


Fig. 3. Relative depth error and relative depth uncertainty for detection of single circular (a) and square (b) particles ([Media 1](#)).

of 9830 (60% of the full scale) and the readout noise is 1% of the full scale. For each particle condition (Fresnel number), 10 such holograms are simulated and processed to investigate the effects of random noises on particle detection. Therefore, a total of 480 holograms are simulated for each shape.

Shown in Fig. 3 is the measurement accuracy of the z location for single circular and square particles. The horizontal axis is the Fresnel number F , which is logarithmically scaled for clarity. The vertical axis $(z_d - z_0)/D_0$ is the relative depth error with respect to the particle diameter, where z_d is the mean value of the depths detected from 10 holograms for each Fresnel number. δ_z is the standard deviation (uncertainty) of depth determination caused by the random noise, which is also nondimensionalized by dividing by the particle diameter. Note, the depth error is the discrepancy between the measured depth and the actual depth, which can be interpreted as a systematic error in z -location measurement. In particle velocity measurements using two sequentially recorded holograms, the calculation of z -displacement by subtraction of depths tends to eliminate the mean depth error, and thus uncertainty in z -velocity measurement is best related to depth uncertainty, δ_z . Particularly, z -velocity uncertainty can be estimated as $2^{1/2} \delta_z / \Delta t$, assuming that the precision of the time interval Δt contributes negligibly to the overall uncertainty. Figure 3 reveals that all methods display a range of conditions where their performance is optimal. For applications of DIH, these results may provide guidance in selecting a reconstruction algorithm which is best suited to the expected particle conditions and desired measurement quantities. Here the results are shown as a function of F , revealing some general trends which are discussed further in the following paragraphs. In addition, a table containing the full simulation results is provided as [Media 1](#).

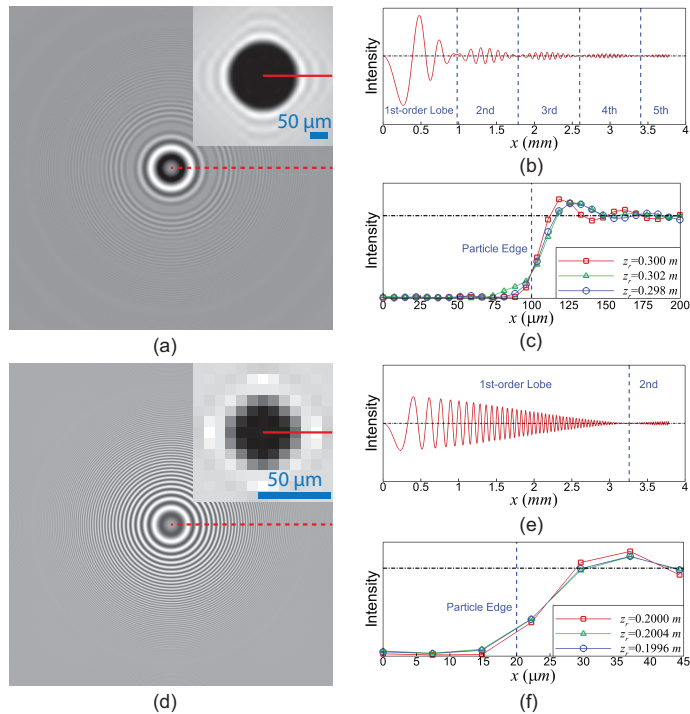


Fig. 4. Illustration of the influence of Fresnel number on particle detection. (a) Hologram simulated at $F = 0.063, D_0 = 200 \mu\text{m}, z_0 = 0.3 \text{ m}$. Inset: particle image obtained by reconstruction of the hologram at $z_r = 0.3 \text{ m}$. (b) Intensity profile along the red dotted line in (a). (c) Intensity profile obtained by reconstruction of the hologram in (a) at $z_r = z_0, z_0 \pm 10D_0$. (d) Hologram simulated at $F = 0.004, D_0 = 40 \mu\text{m}, z_0 = 0.2 \text{ m}$. Inset: particle image obtained by reconstruction of the hologram at $z_r = 0.2 \text{ m}$. (e) Intensity profile along the red dotted line in (d). (f) Intensity profile obtained by reconstruction of the hologram in (d) at $z_r = z_0, z_0 \pm 10D_0$. The visibility of the holograms in (a) and (d) is enhanced for clarity. The hologram dimension is $1024 \times 7.4 \mu\text{m}$. No random noise is included in the simulation.

As shown in Fig. 3, the HYBRID, CC, MINI, and IG methods all perform similarly well when applied to simulated holograms of single circles and squares. For these methods the depth error and uncertainty are generally less than two particle diameters. On the other hand, the LAP, VAR, and MINEI methods display significantly higher errors or uncertainties at certain conditions. While a complete analysis of the root causes of error and uncertainty in all seven methods is beyond the scope of this work, the following discussion attempts to provide initial explanation for some of the trends observed.

Figure 4 shows two hologram simulations. The top row (Figs. 4(a)-4(c)) is for a case of relatively high $F = 0.063$. Figure 4(a) shows the simulated hologram, while Fig. 4(b) shows the radial intensity profile along the dotted line in Fig. 4(a). The inset in Fig. 4(a) shows the reconstructed intensity when the hologram is re-focused to the actual particle position, z_0 , using Eq. (1), while Fig. 4(c) shows the radial intensity profile along the solid line in the re-focused image. In addition, Fig. 4(c) shows the intensity profiles when the hologram is re-focused to $z_r = z_0 \pm 10D_0$ (green and blue lines). Finally, the bottom row (Figs. 4(d)-4(f)) is for a case of relatively low $F = 0.004$ and is displayed in a similar manner.

The LAP and VAR methods both tend to display highest error and uncertainty at lowest F . As the bottom row in Fig. 4 reveals, at small F the interference fringes have a larger radial

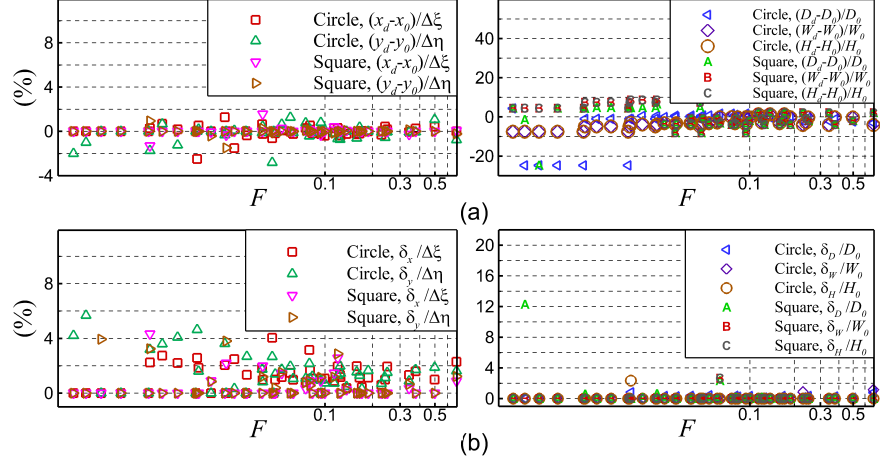


Fig. 5. Relative error of in-plane position and size measurement (a) and relative uncertainty of in-plane position and size measurement (b) for the HYBRID method. W : width; H : height.

extent. Combined with the limited hologram size, this effect results in a decrease of the number of higher-order lobes recorded by the sensor. For example, in Fig. 4(b) at $F = 0.063$ higher-order lobes up to the fifth order are recorded; however, at $F = 0.004$, only part of the second-order lobe is recorded. The loss of higher-order lobes results in less sharp or uniform particle images in reconstruction, as shown in the comparison between the insets in Figs. 4(a) and 4(d). Consequently, focus metrics which rely on edge sharpness (e.g., the LAP method) or particle image uniformity (e.g., the VAR method) tend to display higher uncertainties at lower F .

On the other hand, the MINEI method tends to display higher error and uncertainty at higher F . This method relies on the assumption that pixels on the particle edge experience a minimum in intensity when reconstructed at the actual particle position, z_0 . Figure 4(f) reveals that this is generally true at low F (notice the intensity near the particle edge is minimum when $z_r = z_0$, red line, in comparison to $z_r = z_0 \pm 10D_0$, green and blue lines). In contrast, at higher F Fig. 4(c) reveals that rapid variation in intensity at the particle edge results in some pixels near the border which do not follow this trend. Combined with necessary discretization of the edge region as selected by the MINEI method, this effect tends to increase error in the measured particle depth at higher F .

It is important to retell that this discussion addresses the effect of only one parameter, F , on the method accuracy. In practice it is well known that many other parameters can affect accuracy including the particle diameter/pixel size ratio, signal to noise ratio, particle morphology, position of the particle with respect to the detector edge, laser wavelength and coherence, particle number density, three-dimensionality of the particle fields, particle overlap within the field of view, etc. The results provided in [Media 1](#) can be used to explore some of these effects (such as the particle diameter/pixel size ratio and the particle morphology). In addition, results presented in the proceeding sections use simulations and experiments of particle fields to provide some additional insight into the effects of particle number density, three-dimensionality of the particle field, and particle overlap. Nevertheless, due to the wide range of factors affecting measurement accuracy, caution should be applied before extending any of the results or conclusions presented here to conditions not explored in this work.

Finally, it is noted that, with the exception of the HYBRID method, simulation results presented in this section were calculated using a-priori knowledge of the particle x - y location and

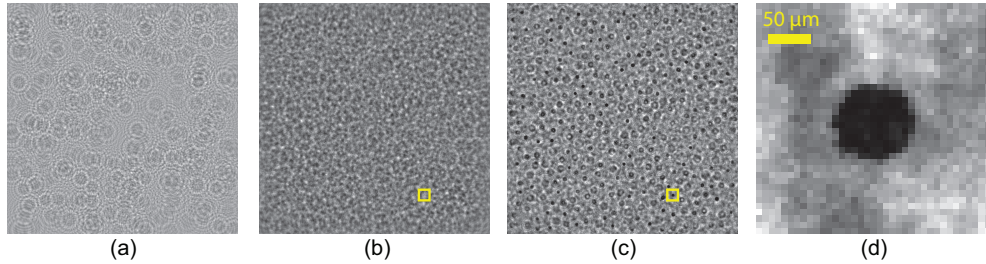


Fig. 6. (a) Example synthetic hologram at $\bar{F} = 0.013$, $\rho_n = 6 \text{ mm}^{-2}$. (b) Example synthetic hologram at $\bar{F} = 0.032$, $\rho_n = 6 \text{ mm}^{-2}$. (c) Reconstruction of the hologram in (b) at the depth of the particle enclosed by the window. (d) Zoomed-in image of the particle enclosed in (c).

shape. In contrast, the HYBRID method has been specifically designed to automatically select thresholds for image segmentation, and therefore can also be used to measure particle x - y location and shape. Figure 5 shows the relative error and uncertainty of these quantities as measured by the HYBRID method for the range of conditions explored in this section. A particle can be located in the x - y plane with sub-pixel accuracy (less than 0.1 pixels). The relative error of size measurement is less than 5%, except at small Fresnel numbers where sizing becomes difficult due to decreased edge sharpness as displayed in the bottom row in Fig. 4. Similar results are given in [22].

5.2. Accuracy in detecting a particle field

In practical applications, instead of a single particle, the object of interest is often a particle field, where light scattered from other particles contributes to the noise, resulting in increased depth errors and uncertainties.

Here, synthetic particles are of spherical shapes and are randomly distributed in a volume of dimensions $7.6 \text{ mm} \times 7.6 \text{ mm} \times 5 \text{ cm}$, where 5 cm is the dimension in the z direction. Dimensions in the x and y directions are determined by the hologram size (1024×1024 with $7.4 \times 7.4 \mu\text{m}^2$ pixels). To exclude the effects of overlapping particles on particle detection accuracy, the particles are separated transversely from each other, such that the minimum in-plane distance between neighbor particle centers is $3D_0$. Particle diameters are normally distributed with a standard deviation of $10 \mu\text{m}$. The mean diameter \bar{D}_0 is $50 \mu\text{m}$ or $100 \mu\text{m}$. The distance between the hologram plane and the nearest surface of the particle volume, L , is 0.06 m or 0.12 m . The particle number density, ρ_n , which is the average number of particles over the cross-section area of the volume, has two values: 3 mm^{-2} and 6 mm^{-2} . Eight different particle fields are generated by varying \bar{D}_0 , L and ρ_n . To simulate the effects of particle displacement between sequentially recorded holograms, six holograms are calculated wherein the particle field is displaced 1 mm in the z direction between each hologram. In total 48 holograms are generated. The wavelength is 532 nm .

The hologram reconstruction equation (Eq. (1)) is applied to simulate holograms of particle fields. First, particles are sorted such that their distances to the hologram plane are arranged in a descending order, e.g., $z_{0,i} > z_{0,i+1}$. The complex amplitude immediately after impinging on the i^{th} particle can be expressed as

$$E_a^{(i)}(k, l) = \mathcal{F}^{-1} \left\{ \mathcal{F}\{E_a^{(i-1)}(k, l)\} G(k', l', z_{0,i-1} - z_{0,i}) \right\} p_i(k, l). \quad (18)$$

Table 1. Error of measured mean displacement, mean relative depth error and relative depth uncertainty for detection of synthetic particle fields.

	$\bar{F} = 0.008$		0.013		0.032		0.054		
	$\rho_n = 3 \text{ (mm}^{-2}\text{)}$		6	3	6	3	6	3	6
Error of Mean Displacement $ \bar{\Delta z}_d - \Delta z_0 \text{ (mm)}$									
HYBRID	0.00	0.00	0.00	0.00	0.00	0.00	0.00	0.00	0.00
LAP	0.00	0.01	0.02	0.00	0.00	0.04	0.01	0.03	
CC	0.00	0.09	0.00	0.00	0.06	0.14	0.11	0.18	
VAR	0.02	0.35	0.22	0.11	0.05	0.01	0.00	0.01	
MINI	0.00	0.00	0.00	0.00	0.00	0.01	0.00	0.00	
MINEI	0.00	0.00	0.00	0.00	0.01	0.00	0.02	0.02	
IG	0.00	0.00	0.00	0.00	0.00	0.00	0.00	0.00	
Mean Relative Depth Error $ \bar{z}_d - z_0 /\bar{D}_0$									
HYBRID	0.94	1.20	0.61	0.80	0.75	0.94	0.71	0.79	
LAP	9.95	9.80	10.68	11.08	7.23	9.47	8.73	9.29	
CC	2.44	5.56	1.41	3.44	22.74	98.47	23.97	63.88	
VAR	252.35	117.31	79.90	29.15	5.79	4.05	0.40	2.37	
MINI	0.44	0.55	0.34	0.41	0.42	0.65	0.39	0.39	
MINEI	2.08	3.18	1.42	2.11	9.26	20.96	5.57	16.80	
IG	0.39	0.44	0.30	0.37	0.28	0.32	0.31	0.29	
Relative Depth Uncertainty δ_z/\bar{D}_0									
HYBRID	0.76	1.19	0.53	0.65	0.31	0.58	0.37	0.67	
LAP	8.76	8.73	10.15	10.73	6.24	20.14	7.69	16.69	
CC	1.88	37.49	1.28	21.17	33.01	64.63	41.59	59.57	
VAR	197.82	160.91	100.36	76.68	21.78	20.41	0.15	9.65	
MINI	0.28	0.33	0.25	0.26	0.15	0.18	0.11	0.14	
MINEI	2.02	2.62	1.71	2.25	3.89	6.35	3.16	5.84	
IG	0.28	0.30	0.22	0.25	0.15	0.16	0.12	0.13	

$$p_i(k, l) = \begin{cases} 0, \sqrt{(k\Delta\xi - x_{0,i})^2 + (l\Delta\eta - y_{0,i})^2} \leq D_{0,i}/2 \\ 1, \sqrt{(k\Delta\xi - x_{0,i})^2 + (l\Delta\eta - y_{0,i})^2} > D_{0,i}/2 \end{cases} \quad (19)$$

is the mask function of the i^{th} particle with diameter $D_{0,i}$ located at $(x_{0,i}, y_{0,i}, z_{0,i})$. $E_a^{(i-1)}(k, l)$ is the complex amplitude right after impinging on the $(i-1)^{th}$ particle, and $E_a^{(1)}(k, l) = p_1(k, l)$, assuming a uniform plane wave impinging on the first particle. Finally, the hologram is obtained by

$$h(m, n) = \left| \mathcal{F}^{-1} \left\{ \mathcal{F} \{ E_a^{(K)}(k, l) \} G(k', l', L) \right\} \right|^2, \quad (20)$$

where K is the number of particles. To alleviate the space-domain aliasing introduced by the inverse FFT operation, the simulation is conducted within a much larger “frame”, and the final hologram is cropped from the center of the larger hologram. Specifically, a 4096×4096 hologram is first simulated, then the 1024×1024 hologram used for uncertainty characterization is cropped from the center. The effects of digital recording are also included in the same manner as in Section 5.1. Two sample synthetic holograms of particle fields are shown in Figs. 6(a) and 6(b). Again, the alternative methods are operated on the exact particle pixels and windows, while the HYBRID method is implemented without knowledge about the particle field. Due to

Table 2. Detection effectiveness and mean size measurement error of the HYBRID method in detection of synthetic particle fields.

	$\bar{F} = 0.008$		0.013		0.032		0.054	
	$\rho_n = 3 \text{ (mm}^{-2}\text{)}$	6	3	6	3	6	3	6
Detection Effectiveness (%)	86.5	86.4	87.2	80.2	100.0	100.0	100.0	99.8
$ D_d - D_0 /D_0$ (%)	5.9	6.5	4.9	4.2	1.7	2.3	0.9	1.8
$ W_d - D_0 /D_0$ (%)	7.5	7.4	6.5	6.4	2.9	3.4	2.9	3.1
$ H_d - D_0 /D_0$ (%)	7.0	7.5	6.4	6.4	2.8	3.5	2.6	3.2

the limited size of the hologram, some fringes are lost for particles close to the borders, leading to inaccurate particle detection. Therefore, for $L = 0.06 \text{ m}$, particles within 50 pixels of the borders are neglected; for $L = 0.12 \text{ m}$, particles within 100 pixels of the borders are neglected. An average Fresnel number \bar{F} can be calculated for each particle field using \bar{D}_0 and the distance between the hologram plane and the particle field center, as shown in the first row of Table 1.

The z locations of the particles identified by the HYBRID method are determined using alternative methods by applying them directly to the exact particle pixels and windows. For each pair of particles in consecutive holograms, an individual displacement Δz_d can be obtained by subtraction of the first depth from the second depth. The standard deviation of displacements detected from all pairs of particles in the five translations is taken as the z -displacement uncertainty, which is then divided by $2^{1/2}$ to obtain the depth measurement uncertainty, δ_z . To evaluate the depth error, the detected depth, z_d , is compared with the particle actual depth, z_0 , and the relative depth error is calculated by $|z_d - z_0|/D_0$. For each particle field, the mean value of Δz_d is computed from all particle pairs in the five translations, and the mean value of $|z_d - z_0|/D_0$ is computed from all detected particles in the six holograms, as listed in Table 1. The relative depth uncertainty is with respect to the mean particle diameter, \bar{D}_0 .

As shown in Table 1, for a given \bar{F} , higher particle number density has negative effects on all particle detection methods, as is expected due to the increased noise introduced by neighboring particles. Similar to the results presented in Section 5.1, Table 1 indicates that the HYBRID, MINI, and IG methods all perform relatively well over the range of conditions explored here. Also, the VAR method is generally less accurate at low \bar{F} , while the MINEI method is less accurate at higher \bar{F} . However, in contrast to the results presented in Section 5.1, the LAP method shows relatively high uncertainty over the entire range of \bar{F} , and the CC method degrades severely at high \bar{F} . Both the LAP and CC methods are performed within windows that enclose target particles, thus noise due to light diffraction from adjacent particles are also included in the window, as shown in the background in Fig. 6(d). It is theorized that the focus metrics of the LAP and CC methods are severely degraded by this noise resulting in the high uncertainty shown in Table 1. Overall, the depth error and uncertainty of the HYBRID method are both less than one particle diameter, while the MINI and IG methods demonstrate superior performance compared to the HYBRID method in terms of smaller depth errors and uncertainties. One is reminded that knowledge of the exact binary images of synthetic particles contribute to their superior performances.

For the HYBRID method, the detection effectiveness is defined as the ratio of the number of detected particles to the total number of particles, which measures the method's capability to automatically extract particles in a particle field. The mean detection effectiveness of the HYBRID method averaged from the six holograms for each particle field is listed in Table 2. The particle size and shape are also measured by the HYBRID method. For each particle field,

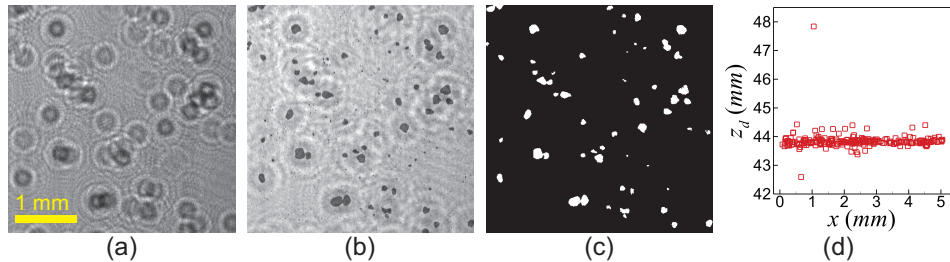


Fig. 7. Illustration of the processing of experimental holograms. (a) sample hologram. (b) reconstructed intensity at the average particle depth. (c) particle binary image extracted by the HYBRID method. (d) depth distribution of detected particles along the x (horizontal) direction. Image contrast is adjusted for better visibility.

mean values of $|D_d - D_0|/D_0$, $|W_d - D_0|/D_0$ and $|H_d - D_0|/D_0$ are calculated from all detected particles in the six holograms, as also listed in Table 2. The relative errors in measurement of the particle diameter, width and height are about 5%, which demonstrates the validity of the particle binary images extracted by the HYBRID method.

6. Quantification of measurement accuracy by experimental holograms

In most experiments involving 3D particle fields, the true x , y , z position of each particle is not known. Therefore, only depth uncertainty, δ_z , can be quantified by processing of sequential holograms of particle fields translated in the z direction.

6.1. Accuracy in detecting a planar particle field

A planar particle field is produced by placing silicon dioxide (S_iO_2) particles on a thin flat glass. The surface of the glass, on which the particles are placed, is perpendicular to the z direction. The glass is further fixed on a translation stage, so that the particle field can be translated to different z positions. The expanded and collimated beam from a He-Ne laser ($\lambda = 632.8\text{ nm}$) is used to illuminate the particle field, and the hologram is recorded by a CCD camera (Cooke pco.2000) with 2048×2048 , $7.4 \times 7.4\text{ }\mu\text{m}^2$ pixels. Most of the particles reside in a region of 1500×700 pixels, which is then cropped from the original size as the hologram. The glass is translated to sequential z positions with a positioning uncertainty of $12.7\text{ }\mu\text{m}$. In an experiment, the glass slide is translated to a total of six different z -positions with uniform spacing, Δz_0 . Two different values of Δz_0 are considered ($127\text{ }\mu\text{m}$ and $635\text{ }\mu\text{m}$), yielding a total of twelve holograms. Particle x - y positions and shapes are measured using the HYBRID method with the lower limit on detectable diameter set to $25\text{ }\mu\text{m}$ (3 pixels). The nominal mean diameter of the S_iO_2 particles is around $40\text{ }\mu\text{m}$. However, due to particle agglomeration and the size threshold, the measured average diameter, \bar{D}_d , is $86\text{ }\mu\text{m}$. The average depth of particles is approximately 4.3 cm . Using these values, an average Fresnel number \bar{F} of 0.065 is found. The particle number density ρ_n is 3.7 mm^{-2} . Shown in Fig. 7 are a part of the hologram, a reconstructed intensity image at the average depth of all particles, the corresponding binary images extracted by the HYBRID method and the depth distribution of the particles measured from one hologram with a standard deviation of $174\text{ }\mu\text{m}$ ($\sim 2\bar{D}_d$).

The detected particles in sequential holograms are matched based on their locations in the x and y directions. Following the accuracy quantification method used in Section 5.2, the mean displacement and depth uncertainty are quantified for each method, as shown in Table 3. The HYBRID, CC, MINI and MINEI methods demonstrate comparable performances. Interestingly, the CC method shows a considerable improvement, which may be attributed to the fact

Table 3. Error of measured mean displacement and relative depth uncertainty for measurement of a planar experimental particle field.

	HYBRID	LAP	CC	VAR	MINI	MINEI	IG
Error of Mean Displacement $ \overline{\Delta z_d} - \Delta z_0 (\mu m)$							
$\Delta z_0 = 127 \mu m$	6	20	1	49	11	11	18
$\Delta z_0 = 635 \mu m$	2	27	6	29	0	7	7
Relative Depth Uncertainty $\delta_z / \overline{D_d}$							
$\Delta z_0 = 127 \mu m$	1.55	10.65	0.97	16.50	2.28	2.39	3.80
$\Delta z_0 = 635 \mu m$	1.55	11.03	1.66	18.93	2.44	2.13	4.18

that the particles are on the same plane, and thus the CC values for each particle tend to reach their maximums at the same z location. Unlike in the processing of synthetic holograms, the exact particle information in experimental holograms is not available to alternative methods. As a result, the MINI and IG methods downgrade from their ideal performances. The LAP and VAR methods display the highest uncertainties.

6.2. Accuracy in detecting a 3D particle field

A 3D particle field is produced by dispersing polystyrene particles in an optical glass cuvette filled with Dow Corning silicone oil. The inner dimensions of the cuvette are also those of the particle field, which are $5 \text{ cm} \times 5 \text{ cm} \times 5 \text{ cm}$. Due to the high viscosity (10000 cSt) of the oil, the particles settle very slowly and can be assumed to be stationary during the duration of an experiment [22]. The cuvette is placed on a translation stage with a positioning uncertainty of $3 \mu m$. In these experiments $\Delta z_0 = 2 \text{ mm}$, and the particle field is displaced seven times in the z direction. The collimated laser beam from a DPSS laser (Coherent Verdi V6, $\lambda = 532 \text{ nm}$) illuminates the particle field, and the resulting hologram is recorded by a CCD camera (Redlake MegaPlus EC16000) with 4872×3248 , $7.4 \times 7.4 \mu m^2$ pixels. To improve statistical convergence, the procedure is repeated after stirring the oil to create a new particle field and degassing in a vacuum to remove any bubbles. In total, fourteen holograms are recorded and processed by the HYBRID method. Particles that are within 200 pixels to the hologram borders are rejected to account for the degradation of accuracy due to loss of diffraction fringes. The particle size distribution is previously measured using a Malvern Mastersizer [22]. Accordingly, the minimum detectable diameter is set to $300 \mu m$ to minimize false particle detection in regions where noise results in local intensity gradients. The average diameter is measured to be $438 \mu m$, close to that measured by the Mastersizer ($450 \mu m$). The average distance between the hologram plane and the cuvette center is about 19.5 cm . Therefore, $\bar{F} = 0.452$ with measured $\rho_n = 0.14 \text{ mm}^{-2}$. Fig. 8 shows a photo of the cuvette filled with silicone oil and particles, a sample region of the hologram and the corresponding particle binary image extracted by the HYBRID method.

The quantified accuracy in terms of mean Δz_d and $\delta_z / \overline{D_d}$ are presented in Table 4. Overlapping particles, as circled in Fig. 8(b), are erroneously detected as single particles with incorrect size and position [22]. A manual refinement, which identifies and removes the overlapping particles, is performed to eliminate the influence of these particles. After this refinement, considerable improvement is observed for most of the methods. Once again, the HYBRID and MINI methods demonstrate the best performance with depth uncertainty less than twice the particle diameter. Compared to the results shown in Section 6.1, the VAR method has a reduced depth uncertainty due to the increase of the Fresnel number, while the IG method has degraded considerably, which may be indicative of its sensitivity to the predetermined particle binary image.

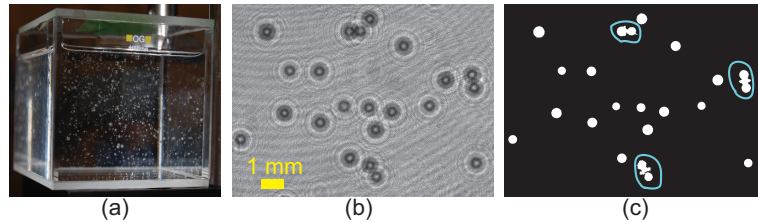


Fig. 8. A photo of the cuvette filled with silicone oil and particles (a), Sample hologram (b) and the corresponding binary image extracted (c). The hologram contrast is adjusted for better visibility.

Table 4. Error of measured mean displacement and relative depth uncertainty for measurement of a 3D experimental particle field after removal of the overlapping particles such as those circled in Fig. 8(c).

	HYBRID	LAP	CC	VAR	MINI	MINEI	IG
$ \bar{\Delta z}_d - \bar{\Delta z}_0 \text{ (mm)}$	0.02	4.99	5.21	0.34	0.02	0.30	6.00
δ_z / \bar{D}_d	1.57	14.61	19.79	3.17	1.84	2.55	14.92

7. Conclusion

Particle depth measurement uncertainties of the HYBRID method and six other methods are quantified using synthetic and experimental holograms. Numerical and experimental conditions are chosen to include or resemble those used in [7, 8, 11, 23], such that the uncertainty quantification results are of relevance to practical applications for particle sizing and tracking. A number of factors which are known to impact the accuracy of particle detection methods are investigated, including the Fresnel number, particle shape, particle number density, three-dimensionality of the particle field and particle overlap in the x - y plane. Note, to allow for accurate sizing, the particle diameter is generally significantly larger than the pixel size for the conditions investigated here. Extension of these results to applications where the particle size is on the order of the pixel size (such as HPIV [17, 26]) is generally not possible.

The performance of the particle detection methods is a strong function of conditions, and each method tends to display a particular range of conditions wherein accuracy is superior. In future applications, these results could be used to select an optimum particle detection method based on the specific conditions expected. In addition, for the range of conditions considered here, the HYBRID method is generally shown to be among the most accurate methods for particle depth measurement, with depth uncertainty less than twice the particle diameter. Unlike other methods, the HYBRID method is also capable of automatic particle segmentation, with a high-degree of accuracy as quantified in this work. Consequently, it is believed that the HYBRID method will be particularly useful for applications to particle tracking and sizing.

Acknowledgments

This work is supported by Sandia National Laboratories, a multiprogram laboratory operated by Sandia Corporation, a Lockheed Martin Company, for the United States Department of Energy's National Nuclear Security Administration under contract No. DE-AC04-94AL85000.